applied optics

Investigation of the broadening effect of ammonia on the S-branch Raman linewidth of nitrogen with time-domain rotational coherent anti-Stokes Raman scattering

Mark Kuria,[1,2] Jonas I. Hölzer,[1,3,*] Henry Misoi,[1,3] Nancy Karuri,[2] and Thomas Seeger[1,3]

[1]Engineering Thermodynamics, University of Siegen, Paul-Bonatz-Str. 9-11, Siegen 57076, Germany
[2]Chemical Engineering Department, Dedan Kimathi University of Technology, Nyeri 10143, Kenya
[3]Center for Sensor Systems ZESS, University of Siegen, Paul-Bonatz-Str. 9-11, Siegen 57076, Germany
*jonas.hoelzer@uni-siegen.de

Received 18 March 2026; revised 7 July 2026; accepted 17 July 2026; posted 20 July 2026; published 7 August 2026

Ammonia (NH_3) emerges as a promising carbon-free, sustainable fuel, but its integration into technical combustion processes requires accurate, spatially, and temporally resolved diagnostics, obtained through non-invasive techniques like rotational coherent anti-Stokes Raman scattering (RCARS). However, the lack of spectroscopic data for ammonia-containing gas mixtures hinders its integration into advanced RCARS spectral models for data evaluation. In this study, we experimentally investigated the broadening effect of NH_3 on the N_2 S-branch Raman linewidths using the picosecond time-resolved RCARS technique. Experiments were conducted on N_2-NH_3 binary mixtures containing up to 50% NH_3, at atmospheric pressure and temperatures up to 870 K close to the ammonia-air autoignition temperature. The peak intensities of the rotational spectrum of NH_3 are weak compared with the N_2 peak intensity and its rotational coherences decay more rapidly than those of N_2, limiting the direct application of NH_3-based RCARS diagnostics in the presence of intense scatterers and complicating its linewidths determination. Nevertheless, NH_3 was found to induce significant broadening of the N_2 Raman lines, which must be quantified to avoid diagnostic errors in RCARS. The magnitude of the S-branch Raman linewidth, obtained from the coherence decay time constant, increases linearly with NH_3 concentration, indicating a more efficient collisional energy transfer in N_2-NH_3 compared to N_2-N_2 collisions. This behavior enables direct determination of N_2-NH_3 broadening coefficients, providing key spectroscopic parameters for RCARS spectral modeling. We further demonstrate that the inclusion of the newly determined linewidth data for nitrogen thermometry prevents temperature errors from inaccurate linewidth approximations. Thus, the obtained N_2-NH_3 broadening coefficients provide the spectroscopic basis for extending RCARS thermometry and species diagnostics to ammonia-fueled combustion and reactive flow environments.

Published by Optica Publishing Group under the terms of the Creative Commons Attribution 4.0 License. Further distribution of this work must maintain attribution to the author(s) and the published article's title, journal citation, and DOI.
https://doi.org/10.1364/AO.599176

1. INTRODUCTION

The growing global emphasis on climate change mitigation has intensified efforts to reduce greenhouse gases (GHGs) emissions by focusing on reducing major contributors such as fossil fuel combustion [1]. Among other proposed mitigation strategies, the use of carbon-free and carbon-neutral fuels is an accepted alternative to fossil fuels. Recent studies have demonstrated that NH_3 can be utilized as a carbon-free fuel in gas turbines, furnaces, and internal combustion engines, hence playing a role in decarbonizing heavy-duty transport and power generation sectors, by retrofitting existing combustion systems [2–5]. Notably, Japan has incorporated NH_3 into its national energy strategy for power generation and maritime applications [6]. However, NH_3 combustion presents several technical challenges, including high NO_x formation, slow flame propagation, high ignition energy requirements, narrow flammability limits, and the risk of unburned NH_3 slip under fuel-rich conditions [7]. These issues necessitate effective control strategies to mitigate toxic emissions while optimizing energy conversion efficiency. Therefore, precise information on the thermodynamic conditions during combustion is essential to optimize

reactive flow and combustion systems with NH_3 as a primary fuel or as part of a fuel blend (e.g., with H_2 or CH_4) to mitigate the current shortcomings of NH_3 combustion.

Coherent anti-Stokes Raman spectroscopy (CARS) is a powerful laser-based diagnostic tool widely recognized for its superior spatial and temporal resolution, making it an essential tool for high-fidelity non-intrusive evaluation of thermodynamic properties [8–11]. It involves a four-wave mixing process by the interaction of three laser beams termed pump, Stokes, and probe, with molecules in the gaseous state to generate a fourth beam, the CARS signal, with encoded information on the interaction environment. The signal has distinct spectral properties that are governed by the third-order non-linear susceptibility ($\chi^{(3)}$), an intrinsic property of the involved molecules [8]. Rotational CARS gives access to the simultaneous evaluation of temperature, species concentration, and pressure with a single laser shot with relative low experimental complexity compared to other CARS techniques providing critical insight into complex reacting environments [8–11]. This is achieved through the application of dual-broadband pump and Stokes beams with a sufficiently high bandwidth to simultaneously excite the entire range of populated rotational coherences from multiple major combustion relevant molecules since they reside within a common spectral range [8].

The rotational CARS spectrum has distinct spectral signatures that are dependent on the temperature, pressure, and species concentration of the molecules in the interaction (probe) volume. Therefore, to decode the information, a spectral contour fitting technique based on a non-linear least-squares algorithm is applied where the rotational CARS spectrum is fitted with a library of theoretically generated spectra [12,13]. The theoretical spectra are computed using molecular spectroscopic parameters obtained under well-defined thermodynamic conditions. The rotational Raman linewidth is an essential parameter that influences the computed spectra, hence the accuracy of the evaluated thermodynamic properties. This is because of its dependence on gas density, temperature, the collisional environment of the probed gas species, and the spectral branch of the observed transition. Regularly applied approximations of unavailable linewidths, for example, by using the ones of a different spectral branch (approximation of the rotational S-branch by vibrational the Q-branch linewidth for RCARS), or omission of the collisional environment in gas mixtures, were shown to result in significant systematic diagnostic errors [14–16]. Therefore, rotational Raman linewidths of the probe molecule in the presence of collider molecules, such as NH_3, must be accurately determined under a variety of conditions. The rotational Raman linewidths can be conveniently obtained from time-resolved RCARS experiments [14].

At atmospheric pressure, the frequency domain linewidth of most molecules is dominated by collisional broadening, which constitutes as a decay of the signal intensity in the time domain. The time-domain experiments involve recording the RCARS spectra at different probe beam delays relative to the excitation (pump and Stokes) beams. The signal intensity $I(t)$ of every isolated rotational transition follows a mono-exponential decay function, which depends on the decay time constant, τ, as described in Eq. (1), where I_0 is the intensity factor, and t is the delay time of the probe beam relative to the time of the excitation beams. For superimposed rotational lines in crowded spectra like oxygen (due to spin-rotation splitting) [17–21] or CO_2 (due to closely spaced hot band lines at elevated temperatures) [22], a beating of the intensity needs to be considered, whose frequency depends on the energy difference between the transitions. This feature can be omitted in this study:

$$I_{J''} = I_0 \exp\left(\frac{-t}{\tau_{J''}}\right). \quad (1)$$

The decay time constant is subsequently used to determine the frequency-domain Lorentzian Raman linewidth, $\Gamma_{J''}$ (FWHM) as expressed in Eq. (2), where c is the speed of light in vacuum and $\tau_{J''}$ corresponds to the decay time constant of the J''th rotational energy level:

$$\Gamma_{J''} = (2\pi c \tau_{J''})^{-1}. \quad (2)$$

The Raman linewidth of every transition in a binary mixture of a species A containing different mole fractions x of the collider M can be described with Eq. (3) by the broadening coefficient $\Gamma_{J'',A-M}$ for the collision pair A-M and the self-broadened linewidth $\Gamma_{J'',A-A}$:

$$\Gamma_{J'',Mix}(x_M) = x_M\left(\Gamma_{J'',A-M} - \Gamma_{J'',A-A}\right) + \Gamma_{J'',A-A}. \quad (3)$$

Equation (3) can also be used to determine the linewidths of a mixture with an arbitrary fraction of x_M of the molecule. This approach can be expanded to multicomponent systems by adding further broadening coefficients weighted by the mole fractions and has demonstrated strong agreement with experimental data in multicomponent systems [23]. For the case of ammonia combustion, self-broadened S-branch Raman linewidths for major molecular species have been extensively characterized under combustion relevant conditions, which include N_2 [14,24–26], O_2 [17–20,24,27,28], and H_2 [29] (present as a co-fuel or from ammonia dissociation [3,30]). Also, the broadening effect by the collisional environment in relevant molecular mixtures of major collider species in ammonia combustion such as N_2-H_2 [15,31], N_2-O_2 [25], N_2-H_2O [32], and O_2-N_2 [20] has been published. Semi-classically calculated ammonia broadening coefficients for the absorption R-branch are reported by Bonamy and Robert [33]. Experimental and theoretical studies for the rovibrational S- and Q-branch broadening for different fundamental bands and collider environments of ammonia can be found in [34–38]. However, to the best of our knowledge, neither the spectral RCARS features of NH_3 have been used for probing, nor has its broadening effect on the other molecular species been studied. The former could facilitate relative N_2-NH_3 concentration determination. Therefore, in this study, we evaluate the possibility of using NH_3 as a probe molecule for RCARS diagnostics and provide the S-branch Raman linewidth of nitrogen including NH_3-broadening effects by time-domain RCARS.

2. EXPERIMENTAL SETUP

This section provides a concise overview of the essential system components of the picosecond time-resolved dual-broadband rotational CARS setup, with particular emphasis on the preparation of N_2-NH_3 mixtures.

A. Laser Setup

Figure 1 shows a schematic of the experimental setup. A neodymium-doped yttrium aluminum garnet (Nd:YAG) laser generates a frequency-doubled beam (shown by the green line) at $\lambda = 532$ nm with a repetition rate of 10 Hz, a pulse energy of 127 mJ, a pulse length of 100 ps, and a spectral bandwidth of approximately 1 cm^{-1} (FWHM). Of this output, 20% are used as the probe beam, while the remaining 80% pumps the broadband dye laser (BBDL). The BBDL generates a broadband beam (shown by the red line) centered at 624 nm, with a bandwidth of ~480 cm^{-1} and a pulse energy of 9 mJ. The pulse length was determined from a delay scan of the non-resonant signal intensity profile of argon to be about 100 ps (FWHM). The red beam is split into pump and Stokes beams, each carrying 50% of the intensity. Glan–Taylor polarizers (GP_1 and GP_2) were introduced into the beam paths of the probe and excitation beams, respectively, to maintain vertical polarization purity. Delay lines (DL_1 and DL_2) were used to adjust the optical path lengths of the probe and Stokes beams, enabling precise temporal overlap of the three input beams. In addition, DL_1 was employed to temporarily delay the probe beam relative to the excitation beams during delay scans. All input beams were focused into the probe volume at the center of an electrically heated furnace chamber using a lens, L_1 ($f = 750$ mm), in a planar BOXCARS geometry.

The generated CARS signal accompanies the pump beam; it is collimated by L_2 ($f = 750$ mm) upon exiting the furnace and isolated from residual beams by a dichroic mirror, DM_2. Residual input beams were guided onto beam dumps (BDs), and the CARS signal was directed through a half-wave plate ($\lambda/2$) to rotate the polarization of the signal to an optimum polarization angle for detection. Neutral density (ND) filters were introduced to attenuate the signal intensity, and the signal was subsequently focused onto the spectrometer slit (width = 250 μm) using L_3 ($f = 100$ mm). The imaging spectrometer ($f = 1000$ mm and 1800 lines/mm grating) was coupled to a front-illuminated CCD camera (4008 × 2688 pixels) for data acquisition. The spectrometer–camera system provided a spectral resolution of 0.23 cm^{-1}/pixel with a horizontal binning of two pixels. For the suppression of the non-resonant background in selected measurements, the polarization angle of the probe beam was rotated using a half-wave plate and a Glan–Taylor polarizer as a polarization analyzer (PA) was introduced in the signal beam path as an analyzer. The polarization angles are provided in Section 3 [39].

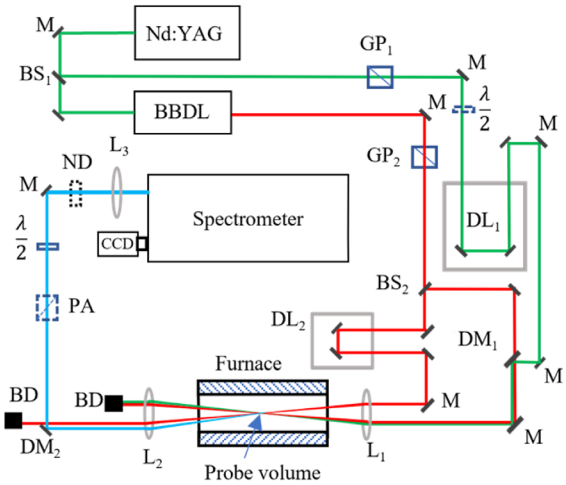

Fig. 1. Schematic of the dual-broadband rotational CARS setup. The 532 nm Nd:YAG beam (in green), the broadband dye laser (BBDL) beam centered at 624 nm (in red), and the generated CARS signal (in blue) are shown, along with key components: $BD_{1,2}$, beam dumps; $BS_{1,2}$, beam splitters; CCD, charge-coupled device camera; $DL_{1,2}$, delay lines; $DM_{1,2}$, dichroic mirrors; $GP_{1,2}$, Glan–Taylor polarizers; PA, polarization analyzer; $\lambda/2$, half-wave plate; $L_{1,2,3}$, lenses; M, mirrors; ND, neutral density filters.

B. Furnace and Gas Mixture Preparation: N_2/NH_3 Mixture Selection and Its Preparation

An electrically heated furnace (Model HTRH 70-150/17, Gero Hochtemperaturöfen GmbH & Co. KG) was used to contain and heat the gas mixture to the desired experimental temperatures. The gaseous mixtures were prepared in accordance with Dalton's law of partial pressures by determining the molecular fractions of each component. Using this technique, the mixtures were prepared at atmospheric pressure for experiments at room temperature, while for high-temperature experiments, they were kept at a slightly lower pressure to accommodate gas expansion during heating.

The experiments were conducted at furnace temperatures of 295, 500, and 870 K for N_2/NH_3 binary mixtures over an NH_3 concentration range of 0%–50% at 1 bar total pressure. The NH_3/N_2 ratio for this upper concentration limit exceeds the ratio at the upper flammability limit of NH_3 in air (a concentration of 25% NH_3 in air corresponds to 30% NH_3 in the binary mixture) [30,40]. Because the upper flammability limit marks the effective concentration limit for ammonia combustion, our dataset provides reliable linewidth data for the most relevant concentration range without the need for extrapolation using Eq. (3). The upper limit of the temperature of 870 K was chosen close to the autoignition temperature (924 K) of NH_3 in air under atmospheric pressure [2,30].

Data for the 50% mixture could not be evaluated at 295 K due to significant stray-light interference even at a reduced total gas density that however vanished at elevated temperatures. Measures to reduce stray light using a short-pass filter or a polarization suppression approach were unsuccessful because either the majority of spectral lines were distorted or signal levels were reduced too much for reliable time-domain evaluation. The output energy of the Nd:YAG laser was continuously monitored throughout data acquisition, with fluctuations remaining within ±2 mJ. The chamber pressure remained stable within ±3 mbar, and the uncertainty in the mixture composition was below 1%. Further information on the optical configuration of the dual-broadband rotational CARS setup, furnace calibration, and mixture preparation can be found in the literature preceding this work [19,25,32].

3. RESULTS AND DISCUSSION

A. Rotational CARS Spectra of Ar-NH_3 and N_2-NH_3 Mixtures

The rotational structure of ammonia is discussed in detail by Herzberg [41]. In brief, NH_3 is a symmetric-top molecule

(point group C_{3v}) whose threefold symmetry axis coincides with an axis of the polarizability ellipsoid. This point group has two rotational motions, which are of A2 and a doubly degenerate E type. Spin statistics in NH_3 yield a 2:1 weight ratio for A2 and E levels. Rotation about the symmetry axis does not result in a change in the induced dipole moment, because the polarizability takes the form of a rotational ellipsoid. As a result, the observable Raman lines follow the selection rules $\Delta J = 0, \pm 1, \pm 2$ (resulting in Q-, R-, and S-branches, respectively) and $\Delta K = 0$, where K is the quantum number associated with angular momentum projection on the principal rotation axis, with the additional restriction that $\Delta J = \pm 1$ transitions are forbidden when $K = 0$ [41]. Due to negligible rotation-vibration coupling, transitions from different K-levels associated with the same J-level coincide spectrally and the spectral separation is dominated by the rotational constant B. Therefore, the spontaneous anti-Stokes Raman spectrum shows two spectral branches (S and R) with every second R-branch peak superimposed by an S-branch line [42–44]. This superposition results in an approximate 2:1 Raman intensity ratio between neighboring peaks. Because of their nature as coincident peaks of different spectral branches, as opposed to, e.g., spin statistics in nitrogen, this intensity ratio strongly changes with temperature and is not constant over the entire spectral range [41].

Figure 2 shows the normalized RCARS spectra of a 70% Ar and 30% NH_3 mixture (blue). Argon was chosen as a non-resonant filler gas. In a second step, argon was replaced by the same mole fraction of nitrogen to evaluate relative signal levels of NH_3 and N_2. The spectrum exhibits an elevated baseline likely due to non-resonant signal contributions from both NH_3 and Ar, indicating a weak absolute signal intensity. The spectral envelope of NH_3 extends from ~ 30 to 280 cm^{-1}. A relative comparison of peak intensities is difficult because of a distinct dispersive line shape feature, resulting from a superposition of the real resonant and non-resonant parts of $\chi^{(3)}$ [8], which is a characteristic of a low resonant to non-resonant signal ratio [8,39].

To obtain an interference-free spectrum, a conventional polarization-based technique was employed to effectively suppress the contribution of the non-resonant background signal. The probe beam was set at 60° linear polarization relative to the excitation beams, and the analyzer was set at −40.9° [45,46]. This achieves optimal resonant signal intensity while significantly reducing, although not eliminating the non-resonant background. The angle for total suppression of the non-resonant signal would have been −60° [39]. The resulting spectrum is shown in the lower panel of Fig. 2 (red). The spectrum now shows two distinct, well-separated sets of peaks, corresponding to the S-branch (with blue tags) and R-branch (with red tags) transitions of NH_3 in the electronic and vibrational ground states, respectively. Coherent addition of S-branch lines with every second R-branch line yields an intensity ratio of approximately 4:1 for the resulting peak, in accordance with the 2:1 ratio found in the spontaneous rotational Raman spectra reported in [42–44]. The observed peak positions and relative intensities are consistent with the rotational Raman structure discussed above. Because several observed features originate from the spectral overlap of transitions belonging to

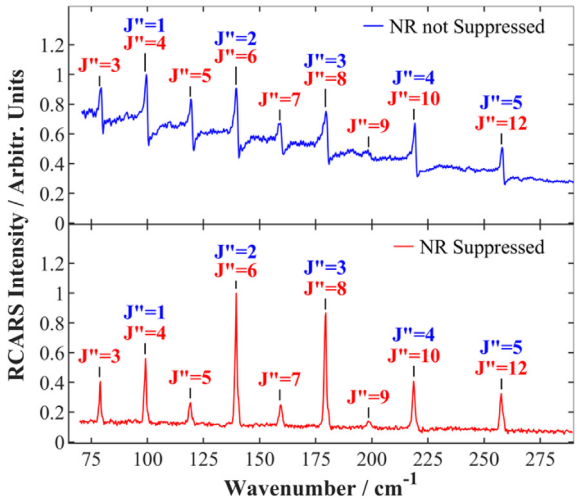

Fig. 2. Normalized rotational CARS spectra of a 70% Ar/30% NH_3 mixture at 295 K and 1 bar, comparing measurements without (blue) and with (red) non-resonant background suppression. The labels indicate the R-branch (blue) and S-branch (red) rotational transitions.

different rotational branches, the relative peak intensities vary across the spectrum and are not expected to remain constant with temperature [40].

To evaluate the relative RCARS intensities of ammonia and nitrogen, Fig. 3 shows normalized RCARS spectra of a 70% N_2/30% NH_3 mixture (blue) without polarization suppression, recorded at 295 K and 1 bar, with the total temporal overlap of the excitation and probe beams (t_0). The NH_3-Ar spectrum from Fig. 2 is shown for reference to identify the NH_3 peak positions. The spectrum of the N_2-NH_3 mixture shows dominant N_2 peaks, with only weakly observable dispersive features of NH_3 and a relatively high contribution of the non-resonant background signal to the spectrum, as shown in the inset of Fig. 3. Ammonia has a significantly larger rotational constant ($B_0 = 9.9443$ cm^{-1} [47]) than N_2 ($B_0 = 1.99824$ cm^{-1} [48]), leading to a larger separation between successive rotational transitions of the same spectral branch. Compared to a hypothetical homonuclear diatomic molecule with the same rotational constant, the maximum of the spectral envelope resides at a larger Raman shift, due to the spectral coincidence of transitions associated with different K-levels having different initial state energies and their population densities [41,44].

We estimated the intensity ratio for pure N_2 and NH_3 based on the polarizability anisotropy γ^2 (computed from polarizability values from [49] to be $\gamma^2_{N_2} = 7.48 \cdot 10^{-25}$ cm^{-3}, $\gamma^2_{NH_3} = 0.576 \cdot 10^{-25}$ cm^{-3}), partition function (at 295 K), and Placzek-Teller coefficients to be 14 for the N_2 $J = 8$ and NH_3 $J = 4$ (the sum over all K for this particular J) peaks. The experimentally determined maximum peak intensity ratio for these peaks after correcting for the 70/30 concentration ratio is 18 ± 9, which agrees well with the estimated theoretical ratio. However, the uncertainty of the experimental value is very high due to the low NH_3 signal intensity and the required correction for the non-resonant background. We are aware that this approximation of relative maximum peak signal intensities of the two molecules in the mixture is not a rigorous determination

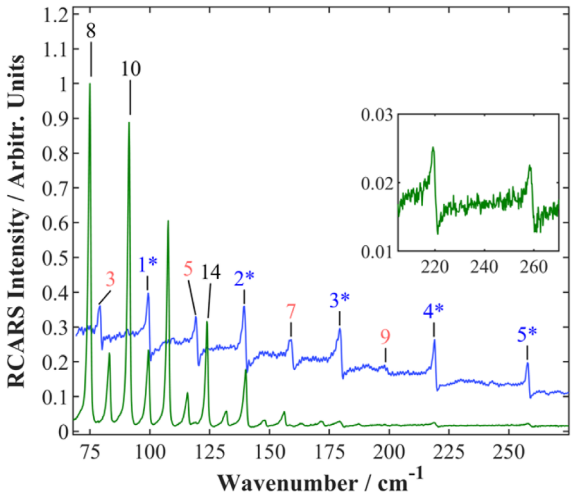

Fig. 3. Normalized RCARS spectrum of a 70% N_2/30% NH_3 mixture (green) recorded at 295 K and 1 bar, at the total temporal overlap of the excitation and probe beams. The spectrum of the 70% Ar/30% NH_3 mixture from Fig. 2 is shown (scaled for visibility) in blue for reference of NH_3 line positions. Tagged spectral peaks correspond to N_2 (black labels) and NH_3 [the R-branch (red labels) and the superimposed R- and S-branch (blue labels with asterisks)]. The inset presents a zoomed-in section between 200 and 270 cm^{-1}, highlighting weak peaks of the 4* and 5* features.

of the intrinsic signal strength. Still, it serves to provide experimentalists with an order-of-magnitude estimation to simplify experimental design. The distinct dispersive features could, in principle, be used for relative concentration determination as demonstrated with vibrational CARS for low concentration CO detection [39]. However, it should be noted that this is likely applicable only to high ammonia mole fractions, as these spectral features are only weakly observable even at a relatively high ammonia fraction. On the other hand, because of the dominance of the N_2 spectral signatures, thermometry is possible without the need to model the spectrum of NH_3, which is more complex due to its nature as a symmetric top molecule, which simplifies evaluation with existing codes.

We conducted a probe delay scan for these mixtures to study the decay behavior. The RCARS intensity generally decreases as the probe beam is delayed relative to the excitation beams. This reduction arises from both the reduction in the temporal overlap of the laser pulses and the decay of the rotational Raman coherence, consistent with observations reported for other molecular systems in time-domain experiments. In our setup, the time at which the non-resonant background has sufficiently decayed to study the collisional coherence decay without interference is about 213 ps [19,25]. However, at this delay, the spectral signatures of NH_3 vanished in the noise floor. This is likely due to a combination of generally low signal levels and rapid dephasing of the excited coherences. The latter is in agreement with the experimental and theoretical microwave, and IR absorption band linewidth data reported for ammonia of about $0.10 - 0.12$ cm^{-1} across different J-levels, vibrational bands, and collider systems at room temperature [33–38]. The corresponding dephasing time constants of 53–44 ps, respectively, result in a monoexponential signal decay by about two orders of magnitude within the aforementioned 213 ps, prohibiting the time-domain determination of the S-branch Raman linewidth of ammonia and decay evaluation. However, recognizing the rapid signal decay of NH_3, it should be studied in the future with shorter excitation pulses and enhanced temporal resolution. The dominant intensity of nitrogen, on the other hand, is strongly visible. Therefore, in the following, only the N_2 spectral peaks and the broadening effect of NH_3 in the N_2-NH_3 binary mixture are investigated.

B. Coherence Decay of Nitrogen Perturbed by Ammonia

Figure 4 shows RCARS signal intensity time traces of N_2 rotational Raman transitions of the selected $J'' = 10$ and $J'' = 18$ in a NH_3-N_2 mixture with 26% NH_3 at 295 and 500 K and 1 bar. The intensity time traces were fitted with a mono-exponential decay function up to around 700 ps, as described by Eq. (1), to determine the coherence decay time constant τ and to assess the collisional effect of NH_3 on N_2. Figure 4 shows that the $J'' = 10$ state exhibits a steeper slope than $J'' = 18$. This corresponds to coherent decay time constants of (48.6 ± 0.3) ps and (66.8 ± 0.6) ps at 295 K, and (72.6 ± 0.4) ps and (87.9 ± 0.6) ps at 500 K, for $J'' = 10$ and $J'' = 18$, respectively. The change of decay time with the rotational quantum number arises from the increasing energy spacing between rotational energy levels with increasing rotational states; as a result, energy transfer is lower due to weaker rotational-translational coupling at higher energy states [50]. Additionally, τ increases with increasing temperature indicating the dependence of the coherence decay time on temperature. This behavior results from the decrease in the gas density of both the probe molecules (N_2) and the colliders (NH_3) at higher temperatures. This reduction in density lowers the number of molecular collisions within the probe volume, leading to longer decay.

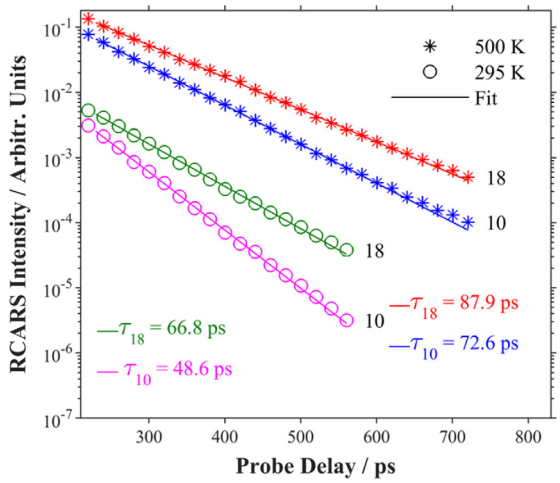

Fig. 4. Normalized time traces of the CARS intensity integrated over a single rotational spectral line as a function of probe delay for $J'' = 10$ and $J'' = 18$ in the N_2-NH_3 binary mixture containing 26% NH_3 at 1 bar and 295 K (circles, scaled down by a factor of 10) and 500 K (asterisks). The data are fitted with mono-exponential decay functions, shown by solid lines, with the resulting decay constants provided in the figure.

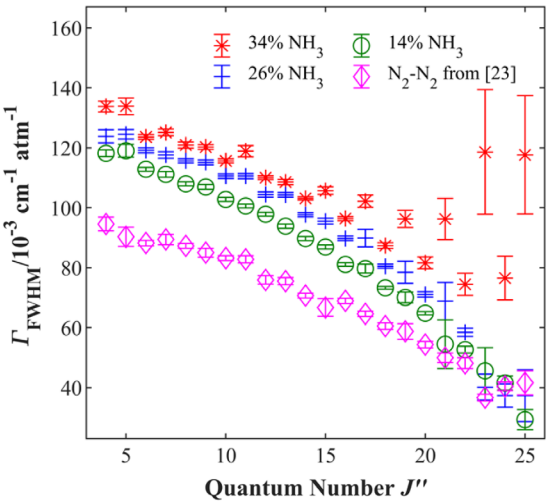

Fig. 5. Nitrogen S-branch Raman linewidths of pure N_2 (in magenta from [25]) and in N_2-NH_3 mixtures with 14% (in green), 26% (in blue), and 34% (in red) NH_3 at a temperature of 295 K.

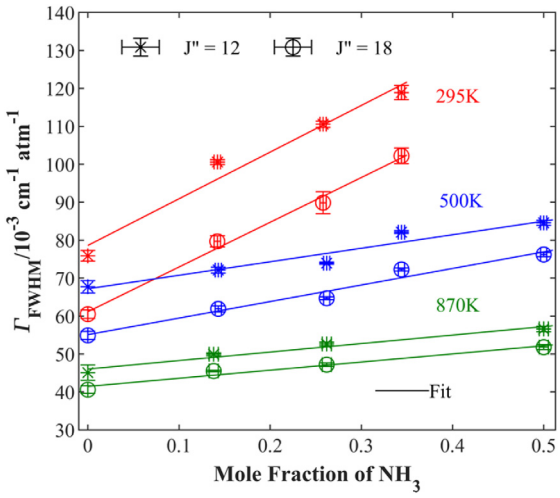

Fig. 6. S-branch Raman linewidths of selected N_2 rotational lines $J'' = 12$ (asterisks) and 18 (circles) in N_2-NH_3 mixtures plotted against the NH_3 mole fraction at 295 K (red), 500 K (blue), and 870 K (green). Data for pure N_2 are from [25]. Fits of Eq. (3) are indicated by solid lines.

C. Determination of N_2-NH_3 S-Branch Raman Linewidths

The frequency-domain S-branch Raman linewidth (Γ) was computed from the experimentally determined coherent decay time constants using Eq. (2) and is shown in Fig. 5. Figure 5 shows the self-broadened S-branch Raman linewidths of N_2 (in magenta) by Meißner *et al*. [25] and N_2 broadened by NH_3 in binary mixtures containing 14% (in green), 26% (in blue), and 34% (in red) NH_3, plotted as a function of the rotational quantum number J'' at 295 K. The error bars in the plot represent the standard deviation of the fitted parameter. The error bars for the higher odd J'' levels are larger particularly at elevated temperatures due to the weaker signal intensity that approaches the noise floor at an earlier delay, reducing the number of data points available for fitting. The presence of NH_3 as a collider molecule influences the coherence decay behavior and hence the Raman linewidth. The binary mixtures exhibit larger Raman linewidths compared to the N_2-N_2 linewidths previously reported by Meißner *et al*. [25] and Kliewer *et al*. [14], with the 34% NH_3 mixture showing the largest observed linewidths. The linewidth magnitude increases systematically with the relative fraction of NH_3, demonstrating a clear correlation with the NH_3 concentration in the mixture. This increase in linewidth results from the accelerated decay, which is attributed to more efficient collisional energy transfer in N_2-NH_3 compared to N_2-N_2 collisions. In addition, the linewidth dependence on J'' changes with increasing NH_3 concentration, with the gradient becoming steeper at higher NH_3 fractions. To quantify the change in magnitude, the linewidths were plotted as a function of ammonia concentration and fitted with Eq. (3).

Figure 6 shows the S-branch Raman linewidths of the selected rotational transitions fitted using Eq. (3) as a function of NH_3 concentration for the three studied temperatures. The fits demonstrate good agreement between the function and the data. The horizontal error bars represent uncertainties in the mixture composition. The broadening coefficient $\Gamma_{N_2-NH_3}$ was determined from the slope of Eq. (3) and is shown in Table 1 for all experimental temperatures. The error bars were determined using the propagation of uncertainty method based on the standard deviation of the fitted parameters and were found to be larger than those derived from the experimental linewidths due to extrapolation. The $\Gamma_{N_2-NH_3}$ coefficient, together with the self-broadening coefficient $\Gamma_{N_2-N_2}$ reported in the literature [14,25,26], can be used to calculate linewidths for arbitrary x_{NH_3} mole fractions in N_2-NH_3 mixtures. It should be noted that extrapolation beyond the experimentally covered 34% and 50% NH_3, respectively, results in a loss of linewidth precision. However, the range of relative N_2/NH_3 fractions studied in our experiments falls within the range relevant for practical combustion applications, because the NH_3/N_2 ratio at the upper flammability limit (25% NH_3 in air) corresponds to an NH_3 concentration of 30% in a binary mixture. As a result, the associated uncertainties remain reasonably low in these relevant concentration ranges and comparable to the experimental uncertainties.

The rotational Raman linewidth of N_2 in the N_2-NH_3 mixtures exhibits similar behavior to that observed in the N_2-H_2O mixtures [32]. In both systems, the linewidth increases with the concentration of the collider molecules. However, NH_3 collisions additionally lead to a visible effect on the J-dependence, which is not present in the H_2O broadened situation [32]. For N_2-NH_3, we investigated the effect on temperature evaluation by inclusion of ammonia broadening using 500 single-shot RCARS spectra of an N_2-NH_3 mixture with 26% NH_3 at a furnace temperature of 500 K and a pressure of 1 bar. The spectra library for the fitting routine was calculated using pure self-broadened nitrogen linewidths and accurate linewidths for this mixture, respectively. Ammonia spectral signatures were not considered. To evaluate the influence of the linewidth on the spectral profile, the best-fit spectrum (at 497 K) is shown with the mean experimental spectrum in Fig. 7 and compared with the spectrum calculated with self-broadened linewidths for the same temperature. The difference shown below is between "mix-spectrum" and "self-broadened spectrum" and illustrates the systematic "shift" of the intensity envelope from

Table 1. N_2-NH_3 Broadening Coefficients

	$\Gamma(N_2 - NH_3, \mathrm{FWHM})/(10^{-3}\ \mathrm{cm}^{-1}/\mathrm{atm})$		
J''	295 K	500 K	870 K
4	255.1 ± 56.5	103.2 ± 17.6	74.7 ± 7.3
5	209.7 ± 23.0	109.7 ± 9.1	81.3 ± 22.9
6	217.0 ± 25.7	112.9 ± 11.1	71.8 ± 11.8
7	188.3 ± 20.2	105.4 ± 4.1	65.4 ± 11.0
8	196.0 ± 17.4	122.9 ± 42.2	60.6 ± 30.6
9	187.9 ± 18.2	103.9 ± 3.6	69.1 ± 6.4
10	191.2 ± 18.4	109.0 ± 5.4	59.6 ± 1.8
11	178.8 ± 13.8	100.9 ± 4.0	63.9 ± 3.2
12	196.7 ± 16.8	103.2 ± 5.5	68.4 ± 5.2
13	174.9 ± 17.4	100.4 ± 6.9	59.6 ± 5.0
14	181.6 ± 17.6	102.7 ± 3.5	61.4 ± 3.0
15	170.3 ± 18.3	103.2 ± 3.8	65.4 ± 2.3
16	174.5 ± 7.0	101.9 ± 3.5	63.4 ± 6.1
17	158.5 ± 7.2	99.8 ± 5.1	64.2 ± 7.3
18	178.0 ± 6.9	98.7 ± 4.1	62.9 ± 4.8
19	143.1 ± 6.4	90.9 ± 5.3	60.4 ± 6.8
20	167.8 ± 14.9	90.0 ± 4.8	61.6 ± 7.3
21	137.3 ± 8.0	92.0 ± 3.8	65.1 ± 5.2
22	169.5 ± 38.0	89.6 ± 3.3	64.1 ± 6.0
23	132.0 ± 18.4	86.1 ± 3.9	58.0 ± 6.4
24		78.1 ± 7.1	63.0 ± 4.5
25		73.0 ± 6.5	62.1 ± 5.9
26		74.9 ± 9.3	61.0 ± 7.3
27			59.2 ± 4.7
28			58.4 ± 8.3
29			52.3 ± 3.0
30			60.1 ± 9.5

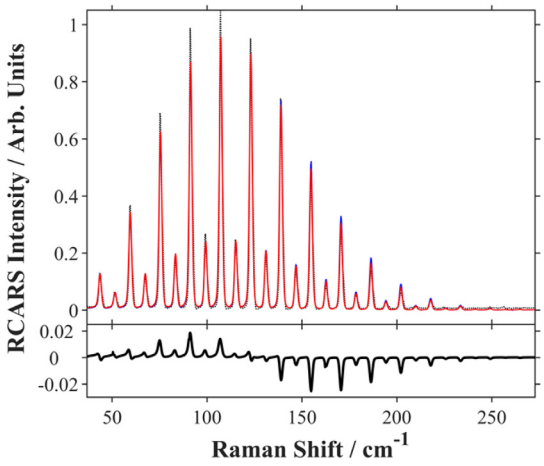

Fig. 7. Experimental S-branch RCARS spectrum (mean of 500 single shots) of a mixture of nitrogen with 26% NH_3 at 500 K and 1 bar (black dotted line) and the best-fit theoretical spectrum incorporating ammonia broadened nitrogen linewidths (red). For comparison, the theoretical spectrum calculated with pure self-broadening at the same temperature is shown (blue). Below, the difference between the two theoretical spectra ("mix"–"self") is shown.

lower to higher Raman shifts when approximating the accurate linewidth by self-broadening for the same temperature. Therefore, fitting results in a systematic temperature bias toward lower temperatures. The evaluated temperature from 500 single shots with ammonia broadening is (497 ± 65) K, which agrees well with the set furnace temperature, while the self-broadened approximation yields (486 ± 64) K. This difference of 11 K (approx. 2%) is smaller than the standard deviation of RCARS thermometry, but it represents systematic bias of the mean, because of the systemic influence on the spectral envelope. This trend is opposite to the effect from N_2-H_2O collisions and underlines the considerable influence of small modifications of the J-dependence of the linewidths.

The newly obtained linewidth data are particularly relevant for nitrogen-based RCARS thermometry in combustion involving ammonia as a fuel or as part of a fuel blend. Although the spectral signatures of ammonia are too weak to be usable for the determination of the mixture composition in the combustion relevant concentration regime, the now available linewidths may still facilitate relative concentration determination. Because the decay behavior is influenced by ammonia molecules in the mixture, simultaneously monitoring the spectrum and the decay behavior gives access to temperature and ammonia concentration as was demonstrated by Castellanos *et al*. for relative N_2/H_2O fractions [51].

4. CONCLUSION

This study systematically investigated the S-branch Raman linewidth of nitrogen broadened by ammonia in gas-phase mixtures using time-domain RCARS in an electrically heated furnace. The spectra of ammonia exhibited low peak signal intensity compared to N_2 and short coherence dephasing time, hampering time-domain measurements. Determination of the decay times and the linewidths of ammonia was not possible due to the rapid signal decay. This necessitates the use of shorter excitation laser pulses with enhanced temporal resolution. The spectral signatures of ammonia are only weakly observable in the presence of the intense N_2 spectrum, rendering relative concentration determination from spectral fitting difficult under technically relevant combustion conditions (i.e., in the presence of strong RCARS scatterers like O_2 and N_2). Still, optimized NH_3-based RCARS diagnostics may provide a useful starting point for future investigation of NH_3 processes such as Haber–Bosch synthesis, ammonia slip monitoring, or plasma-assisted ammonia synthesis. Hence, we focused on the study of the line broadening effect of ammonia on the nitrogen spectrum. The coherent decay time constant of each nitrogen line was determined from the temporal evolution of the RCARS signal intensity and subsequently used to calculate the linewidth. The N_2-NH_3 broadening coefficient was obtained. The S-branch Raman linewidth demonstrated notable variation from self-broadening in both magnitude and slope across different ammonia concentrations. Specifically, both the magnitude and the slope of the linewidth increased with increasing NH_3 concentration, suggesting that collisional energy transfer is more efficient in N_2-NH_3 than in N_2-N_2 collisions. We demonstrate that the newly obtained accurate S-branch Raman linewidth data including ammonia broadening improve temperature determination, by avoiding a systemic bias toward to low temperatures from the self-broadening approximation. This advancement is expected to enhance the accuracy

of thermometry in combustion and reactive flow processes involving NH_3.

Funding. Deutsche Forschungsgemeinschaft (SE804/6-3); Erasmus+ (KA171 International Credit Mobility).

Disclosures. The authors declare that there are no conflicts of interest related to this paper.

Data availability. Data underlying the results presented in this paper are not publicly available at this time but may be obtained from the authors upon reasonable request.

REFERENCES

1. K. Calvin, D. Dasgupta, G. Krinner, *et al.*, "Climate Change 2023: Synthesis Report. Contribution of Working Groups I, II and III to the Sixth Assessment Report of the Intergovernmental Panel on Climate Change [Core Writing Team, H. Lee and J. Romero (Eds.)]," in *1st Intergovernmental Panel on Climate Change (IPCC)*, Geneva, Switzerland, 2023.
2. A. Valera-Medina, H. Xiao, M. Owen-Jones, *et al.*, "Ammonia for power," Prog. Energy Combust. Sci. **69**, 63–102 (2018).
3. A. Valera-Medina, M. Gutesa, H. Xiao, *et al.*, "Premixed ammonia/hydrogen swirl combustion under rich fuel conditions for gas turbines operation," Int. J. Hydrog. Energy **44**, 8615–8626 (2019).
4. J. S. Cardoso, V. Silva, R. C. Rocha, *et al.*, "Ammonia as an energy vector: current and future prospects for low-carbon fuel applications in internal combustion engines," J. Clean. Prod. **296**, 126562 (2021).
5. T. F. Guiberti, G. Pezzella, A. Hayakawa, *et al.*, "Mini review of ammonia for power and propulsion: advances and perspectives," Energy Fuels **37**, 14538–14555 (2023).
6. M. Nagashima, *Japan's Hydrogen Strategy and Its Economic and Geopolitical Implications* (IFRI, 2018).
7. Z. Wei, G. Huang, G. Zeng, *et al.*, "Experimental investigation on emission characteristics of laminar premixed CH_4-NH_3 jet impinging flames across a wide range of conditions," J. Energy Inst. **124**, 102392 (2026).
8. A. C. Eckbreth, *Laser Diagnostics for Combustion Temperature and Species*, 2nd ed., Vol. **3** of Combustion Science and Technology Book Series (Gordon and Breach, 1996).
9. S. Roy, J. R. Gord, and A. K. Patnaik, "Recent advances in coherent anti-Stokes Raman scattering spectroscopy: fundamental developments and applications in reacting flows," Prog. Energy Combust. Sci. **36**, 280–306 (2010).
10. A. Ehn, J. Zhu, X. Li, *et al.*, "Advanced laser-based techniques for gas-phase diagnostics in combustion and aerospace engineering," Appl. Spectrosc. **71**, 341–366 (2017).
11. M. Aldén, "Spatially and temporally resolved laser/optical diagnostics of combustion processes: from fundamentals to practical applications," Proc. Combust. Inst. **39**, 1185–1228 (2023).
12. R. E. Palmer, "The CARSFT computer code calculating coherent anti-Stokes Raman spectra: user and programmer information," SAND89-8206 (1989).
13. E. Magens, *Nutzung von Rotations-CARS zur Temperatur- und Konzentrationsmessung in Flammen* (Friedrich-Alexander-Universität Erlangen-Nürnberg, 1993).
14. C. J. Kliewer, A. Bohlin, E. Nordström, *et al.*, "Time-domain measurements of S-branch N_2–N_2 Raman linewidths using picosecond pure rotational coherent anti-Stokes Raman spectroscopy," Appl. Phys. B **108**, 419–426 (2012).
15. A. Bohlin, E. Nordström, B. D. Patterson, *et al.*, "Direct measurement of S-branch N_2-H_2 Raman linewidths using time-resolved pure rotational coherent anti-Stokes Raman spectroscopy," J. Chem. Phys. **137**, 074302 (2012).
16. J. I. Hölzer, H. Misoi, and T. Seeger, "Systematic temperature error in RCARS diagnostics from improper Raman linewidths," Proc. Combust. Inst. **41**, 105842 (2025).
17. A. A. Milner, A. Korobenko, and V. Milner, "Coherent spin–rotational dynamics of oxygen superrotors," New J. Phys. **16**, 093038 (2014).
18. T. L. Courtney and C. J. Kliewer, "Rotational coherence beating in molecular oxygen: coupling between electronic spin and nuclear angular momenta," J. Chem. Phys. **149**, 234201 (2018).
19. J. I. Hölzer, C. Meißner, and T. Seeger, "Oxygen rotational Raman linewidth determination considering nonmonoexponential decoherence behavior," J. Raman Spectrosc. **50**, 1260–1267 (2019).
20. J. I. Hölzer, C. Meißner, and T. Seeger, "Improvement of the coherent model function for S-branch Raman linewidth determination in oxygen," Appl. Opt. **60**, C76–C83 (2021).
21. H. Misoi, J. I. Hölzer, and T. Seeger, "Temperature dependent determination of the S-branch Raman linewidths of oxygen and carbon dioxide in an oxyfuel relevant mixture," Appl. Opt. **60**, 4410–4417 (2021).
22. H. Misoi, J. Muriithi, J. I. Hölzer, *et al.*, "Temperature-dependent investigation of the S-branch Raman linewidth in CO_2 via time-resolved rotational CARS," J. Raman Spectrosc. **57**, 725–734 (2025).
23. J. Bonamy, D. Robert, J. M. Hartmann, *et al.*, "Line broadening, line shifting, and line coupling effects on N_2–H_2O stimulated Raman spectra," J. Chem. Phys. **91**, 5916–5925 (1989).
24. J. D. Miller, S. Roy, J. R. Gord, *et al.*, "Communication: time-domain measurement of high-pressure N_2 and O_2 self-broadened linewidths using hybrid femtosecond/picosecond coherent anti-Stokes Raman scattering," J. Chem. Phys. **135**, 201104 (2011).
25. C. Meißner, J. I. Hölzer, and T. Seeger, "Determination of N_2–N_2 and N_2–O_2 S-branch Raman linewidths using time-resolved picosecond pure rotational coherent anti-Stokes Raman scattering," Appl. Opt. **58**, C47–C54 (2019).
26. M. Linne, N. T. Mecker, C. J. Kliewer, *et al.*, "Revisiting N_2-N_2 collisional linewidth models for S-branch rotational Raman scattering," Combust. Flame **243**, 111928 (2021).
27. K. S. Jammu, G. E. St. John, and H. L. Welsh, "Pressure broadening of the rotational Raman lines of some simple gases," Can. J. Phys. **44**, 797–814 (1966).
28. J. P. Looney and G. J. Rosasco, "Semiclassical calculation of self-broadening in O_2, N_2, and CO Raman spectra," J. Chem. Phys. **95**, 2379–2390 (1991).
29. V. G. Arakcheev, D. V. Jakovlev, V. B. Morozov, *et al.*, "Rotational time-domain CARS in H_2: departure from statistically independent collisional dephasing model," J. Raman Spectrosc. **34**, 977–982 (2003).
30. H. Kobayashi, A. Hayakawa, K. D. K. A. Somarathne, *et al.*, "Science and technology of ammonia combustion," Proc. Combust. Inst. **37**, 109–133 (2019).
31. M. Dhyne, M. Lepère, and P. Joubert, "Semiclassical line broadening calculations, using an *ab initio* potential energy surface, in Q-branch and S-branch of N_2 perturbed by H_2," J. Raman Spectrosc. **43**, 2008–2014 (2012).
32. H. Misoi, J. I. Hölzer, and T. Seeger, "Experimental determination of the temperature-dependent broadening effect of water vapour on the S-branch Raman linewidths of nitrogen," J. Raman Spectrosc. **56**, 57–66 (2025).
33. J. Bonamy and D. Robert, "Pressure broadening mechanisms of the ammonia lines: rotation, inversion and rotation-inversion spectra of NH_3 perturbed by monoatomic gases," J. Quant. Spectrosc. Radiat. Transf. **15**, 855–862 (1975).
34. A. S. Pine, V. N. Markov, G. Buffa, *et al.*, "N_2, O_2, H_2, Ar and He broadening in the ν_1 band of NH_3," J. Quant. Spectrosc. Radiat. Transf. **50**, 337–348 (1993).
35. M. Dhib, J.-P. Bouanich, H. Aroui, *et al.*, "Collisional broadening coefficients in the ν_4 band of NH_3 perturbed by He and Ar," J. Mol. Spectrosc. **202**, 83–88 (2000).
36. M. Dhib, J.-P. Bouanich, H. Aroui, *et al.*, "Analysis of N_2, O_2, CO_2, and air broadening of infrared spectral lines in the ν_4 band of NH_3," J. Quant. Spectrosc. Radiat. Transf. **68**, 163–178 (2001).
37. M. Dhib, "Linewidths of ammonia in collisions with He: calculations from an ab initio potential," J. Mol. Spectrosc. **259**, 80–85 (2010).
38. C. Ayari, J. Loreau, M. Dhib, *et al.*, "Semiclassical line broadening calculations using an ab initio potential. Application to NH_3 perturbed by argon," J. Mol. Spectrosc. **318**, 46–52 (2015).

39. A. C. Eckbreth and R. J. Hall, "CARS concentration sensitivity with and without nonresonant background suppression," Combust. Sci. Technol. **25**, 175–192 (1981).
40. Q. Cheng, A. Muhammad, O. Kaario, *et al.*, "Ammonia as a sustainable fuel: review and novel strategies," Renew. Sustain. Energ. Rev. **207**, 114995 (2025).
41. G. Herzberg, *Infrared and Raman Spectra of Polyatomic Molecules*, Vol. **2** of Molecular Spectra and Molecular Structure (Krieger, 1991) [Reprint ed. with corr].
42. R. G. Dickinson, R. T. Dillon, and F. Rasetti, "Raman spectra of polyatomic gases," Phys. Rev. **34**, 582–589 (1929).
43. E. Amaldi and G. Placzek, "Über das Ramanspektrum des gasförmigen Ammoniaks," Z. Phys. **81**, 259–269 (1933).
44. C. M. Lewis and W. V. Houston, "The Raman effect in ammonia and some other gases," Phys. Rev. **44**, 903–910 (1933).
45. F. Vestin, M. Afzelius, and P.-E. Bengtsson, "Development of rotational CARS for combustion diagnostics using a polarization approach," Proc. Combust. Inst. **31**, 833–840 (2007).
46. C. J. Kliewer, Y. Gao, T. Seeger, *et al.*, "Picosecond time-resolved pure-rotational coherent anti-Stokes Raman spectroscopy in sooting flames," Proc. Combust. Inst. **33**, 831–838 (2011).
47. G. Herzberg, *Electronic Spectra and Electronic Structure of Polyatomic Molecules*, 2nd ed., Vol. **3** of Molecular Spectra and Molecular Structure (Krieger, 1991) [reprint ed. with corr].
48. G. Rouillé, G. Millot, R. Saint-Loup, *et al.*, "High-resolution stimulated Raman spectroscopy of O_2," J. Mol. Spectrosc. **154**, 372–382 (1992).
49. J. O. Hirschfelder, C. F. Curtiss, and R. B. Bird, *Molecular Theory of Gases and Liquids* (Wiley, 2010) [Corrected printing with notes added].
50. J. C. Polanyi and K. B. Woodall, "Mechanism of rotational relaxation," J. Chem. Phys. **56**, 1563–1572 (1972).
51. L. Castellanos, F. Mazza, and A. Bohlin, "Water vapor in hydrogen flames measured by time-resolved collisional dephasing of the pure-rotational N_2 CARS signal," Proc. Combust. Inst. **39**, 1279–1287 (2022).